AIAA JOURNAL
Vol. 36, No. 11, November 1998

Compressor Cascade Flow with Strong Shock-Wave/Boundary-Layer Interaction

B. Küsters* and H. A. Schreiber*
German Aerospace Center, 51147 Cologne, Germany

A two-dimensional multiblock Navier–Stokes solver has been successfully applied to a supersonic compressor cascade flow with strong shock-wave/boundary-layer interaction. The cascade model investigated is typical of a fan blade section with precompression design, low flow turning, and a static pressure ratio around 2.0. Numerical calculations have been performed on a very fine grid to guarantee sufficient resolution of the supersonic/transonic flowfield with a complex wave pattern and shock-induced boundary-layer separation. High accuracy and robustness of the numerical scheme is achieved by the second-order Roe upwind–total variation diminishing scheme and a one-equation turbulence model. Investigations were performed for inlet Mach numbers from 1.28 to 1.53 and a Reynolds number of 2.6×10^6. The results are compared with those of previous experiments in a supersonic cascade wind tunnel that provide profile Mach number distributions, wake traverse data, and measured suction surface boundary-layer profiles throughout the strong interaction region. Furthermore, calculated discontinuities of Mach number and flow direction across the shock system at blade passage entrance are compared with laser anemometer data. Finally the influence of inlet Mach number and axial stream tube thickness variation on the shock-wave/boundary-layer interaction mechanism and blade performance is presented.

Nomenclature

AVDR	= axial velocity density ratio, $(\rho_2 w_2 \sin\beta_2)/(\rho_1 w_1 \sin\beta_1)$
c	= profile chord length, 170 mm
c_{ax}	= axial profile chord length, 89.83 mm
H_{12C}	= compressible boundary-layer shape factor, δ_1/δ_2
M	= Mach number
p	= pressure
Re	= Reynolds number, $w_1 c/\nu_1$
t	= blade spacing
w	= velocity
x	= coordinate in chordwise direction
x_0	= start of shock wave interaction
Y'	= distance from blade suction surface in direction normal to $\beta = 150$ deg
β	= flow angle with respect to cascade front
δ_1	= displacement thickness
δ_2	= momentum thickness
η	= coordinate in tangential direction
ν	= kinematic viscosity
ν	= Prandtl–Meyer angle
ξ	= coordinate in axial direction
ρ	= density
ω	= total pressure loss coefficient, $(p_{t1} - p_{t2})/(p_{t1} - p_1)$

Subscripts

is	= isentropic entity
t	= total
1	= inlet plane
2	= exit plane

Introduction

FAN and compressor designs are constantly being pushed to higher pressure ratios and lower weights. This leads to a considerable increase in the flow velocities relative to the blades with supersonic speeds and shock waves in front of and within the blade passages. To realize the full benefit of such high-speed compressors for increased pressure ratios and a reduced number of stages without compromising the efficiency level, a profound understanding of the flow phenomena and loss mechanism of the transonic blade-to-blade flow is necessary. At transonic and supersonic inflow conditions, the blade pressure rise and blade element efficiency are essentially dependent on both the shock strength and the interaction mechanism of the shock waves with the blade surface boundary layer. Many of the former and recent experimental and numerical investigations deal with the interaction between a normal shock wave and a turbulent boundary layer with preshock Mach numbers sufficiently high to cause separation.[1,2] These studies, however, were performed on very simple models like flat plates or bumps on wind-tunnel walls with little or no adverse pressure gradient downstream of the interaction. Little information is available from corresponding studies on real turbomachinery blade elements.[3] In previous papers by Schreiber,[4,5] however, detailed experimental results are presented, which have been obtained from a compressor cascade model investigated in the supersonic cascade facility of the DLR Cologne. These papers provide a thorough description of blade performance, the shock wave pattern, and the flow physics associated with shock-induced separation for inlet Mach numbers from 1.28 to 1.6. Numerical simulation, as well as experiments, is becoming a more and more important and reliable tool to analyze transonic flow phenomena in turbomachines or to perform parameter studies during the design process.[6] The goal of the present research is to simulate and to understand the transonic flow phenomena in a highly loaded compressor cascade. A Navier–Stokes solver, which has already been applied to other complex flows,[7,8] is validated using the data of several tests, which provide blade surface pressures, overall performance from wake traverses, and detailed suction surface boundary-layer data throughout the shock interaction region. Emphasis is placed on a very fine resolution of the flowfield to give a sharp reproduction of the embedded shock waves and an accurate simulation of the boundary-layer development.

Cascade Model

The cascade model shown in Fig. 1 is typical of a fan blade element with supersonic inflow and low turning. It was designed especially for the experimental investigation of a strong shock-wave/boundary-layer interaction (SWBLI) on the blade suction surface.[4] To reduce the preshock Mach number at the blade passage entrance, the blade was designed with a concave suction surface curvature in the front portion up to 18% of chord. At the design inlet Mach number of 1.5, the Mach number incident to the first oblique passage

Presented as Paper 97-2882 at the AIAA/ASME/SAE/ASEE 33rd Joint Propulsion Conference, Seattle, WA, July 6–9, 1997; received Nov. 26, 1997; revision received July 6, 1998; accepted for publication July 26, 1998.

*Research Engineer, Institute of Propulsion Technology, Linder Höhe.

shock could be reduced to 1.4 and does not exceed a value of 1.52 near the blade contour. At the design pressure ratio of 2.2, however, the first relatively strong oblique passage shock, which meets the blade surface at about 63% of chord, induces a severe boundary-layer separation. Because of the separation, a lambda shock develops and a typical Mach reflection of the oblique shock forms inside the blade passage. Corresponding wave pattern and calculated Mach number contours are shown in Fig. 2.

The tests have been performed with a blade chord of 170 mm, giving a Reynolds number of about 2.6×10^6. Because of natural transition occurring within the precompression region on the suction surface, the boundary layer ahead of the strong interaction is turbulent.

Flow Solver and Computational Domain

The computational domain of the simulation extends from $-0.76c_{ax} \leq \xi \leq 2.27c_{ax}$, where $\xi = 0$ corresponds to the blade leading edge. A multiblock grid with one O-block around the blade and four I-blocks was used with a total of 31,781 nodes. First grid spacing normal to the blade surface was 0.00003 chord. This yielded values of $y^+ \approx 1.6$ and about 25 grid nodes within the boundary layer near the interaction region. The DLR-TRACE-U code,[7,8] which has been especially developed to investigate steady and unsteady flow phenomena in turbomachines, has been used to perform the calculations. It allows multiblock grids, and it is possible to perform two-dimensional or three-dimensional, steady or unsteady multistage calculations. Within the code, various numerical methods are implemented and can easily be exchanged. The essential ones used for the present two-dimensional steady-state calculations are as follows: The two-dimensional Reynolds-averaged Navier–Stokes equations are solved for a compressible ideal gas in conjunction with an eddy viscosity model. Convective fluxes are discretized using a second-order Roe upwind–total variation diminishing (TVD) scheme,[9,10] and the viscous fluxes are discretized using central differences. The turbulence model used for the calculations is the one-equation approach developed by Spalart and Allmaras.[11] The simulation was performed with a fully turbulent boundary layer on both the suction and pressure side. Inlet and exit boundaries are treated by nonreflecting boundary conditions according to Giles[12] and modified by Engel et al.[13] For supersonic inlet Mach numbers but still axially subsonic flow, they allow one to specify the incoming nonlinear supersonic Riemann invariants. By specifying $\beta_1 + \nu(M_1) = \text{const}$, the inlet flow angle becomes an outcome of the solution. To simulate an axial stream tube variation, a linear stream tube thickness distribution from the leading-edge to the trailing-edge plane has been assumed. Spatial discretization is combined with a modified four-stage Runge–Kutta time-stepping scheme. Implicit residual smoothing and local time stepping are used to accelerate convergence. This yielded a converged solution normally within 6000 iterations from the initial state.

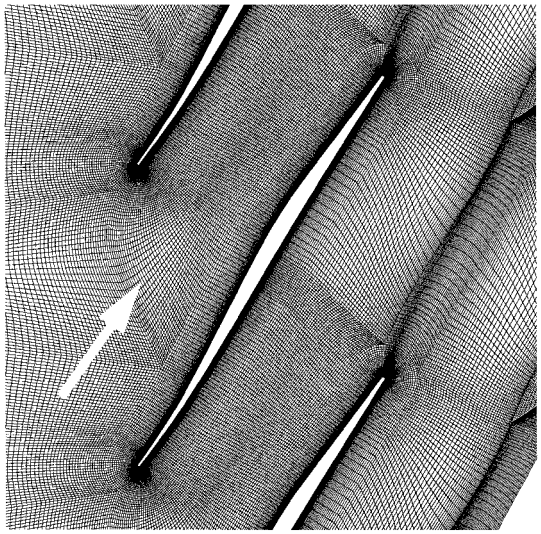

Chord	c	=	170 mm
Thickness	d_{max}/c	=	0.03
Gap-chord ratio	t/c	=	0.65
Stagger angle	β_s	=	148.1°
Reynolds number	Re	=	$2.6*10^6$

Fig. 1 Cascade and computational grid.

Discussion of Results

Inlet and outlet flow conditions and results, such as the total pressure loss coefficient and pressure ratio, of the flow cases presented here are listed in Table 1 in comparison to corresponding experimental results.

Inlet Mach Number $M_1 = 1.5$

As a first example, a test case was selected with flow conditions near design and virtually no stream tube thickness variation [axial velocity density ratio (AVDR) ≈ 1.0]. Mach number contours and profile isentropic Mach number distributions are shown in Fig. 2. With the supersonic but axially subsonic inlet flow, the cascade operates at unique incidence, and the upstream flowfield is independent of the prescribed back pressure. For calculating the flowfield, the exit pressure and the linear stream tube thickness variation (AVDR) were set in such a way that the isentropic Mach number distributions and in particular the shock locations showed best agreement. This ensures that the boundary-layer loading within the interaction region is nearly identical for the experiment and the numerical simulation, allowing a detailed comparison of the local phenomena. The

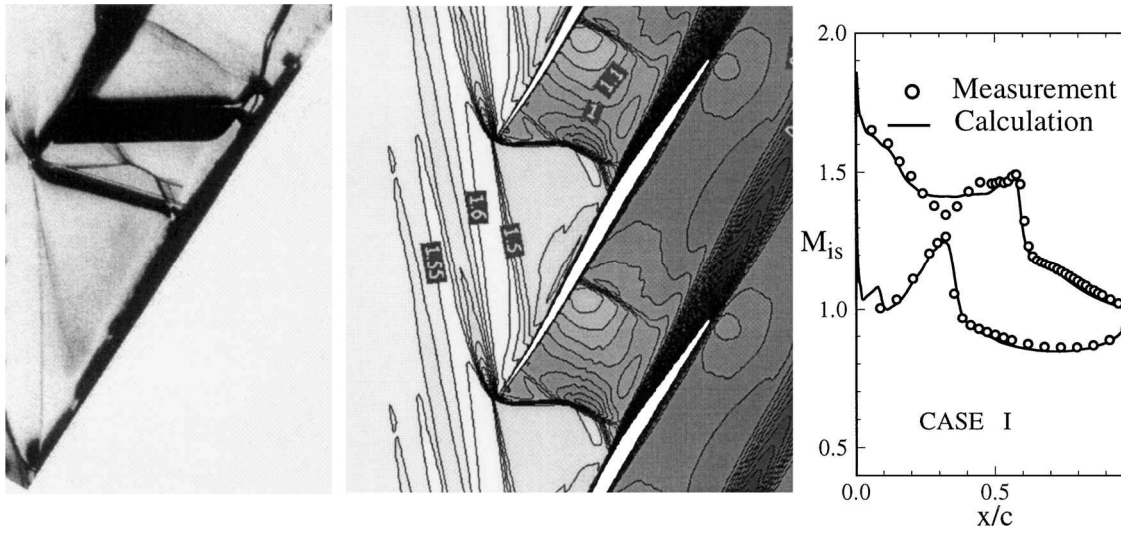

Fig. 2 Experimental schlieren picture, calculated Mach number contours, and profile Mach number distribution at $M_1 = 1.5$ and $p_2/p_1 = 2.28$.

Table 1 Calculation and measurement data

	Case							
	1, $M_1 = 1.5$		2, $M_1 = 1.43$		3, $M_1 = 1.37$		4, $M_1 = 1.53$	
Parameter	Measurement	Calculation	Measurement	Calculation	Measurement	Calculation	Measurement	Calculation
M_1	1.49	1.51	1.43	1.43	1.37	1.37	1.53	1.53
β_1	150.0	149.5	150.5	151.0	150.6	150.8	149.9	149.4
AVDR	1.00	0.94	1.06	1.06	1.02	1.02	1.02	0.96
M_2	0.78	0.75	0.72	0.74	0.71	0.71	0.85	0.81
β_2	150.3	151.8	148.0	148.6	148.4	148.6	150.8	152.2
p_2/p_1	2.20	2.28	2.19	2.15	2.06	2.06	2.13	2.30
ω	0.131	0.136	0.097	0.096	0.080	0.088	0.144	0.140

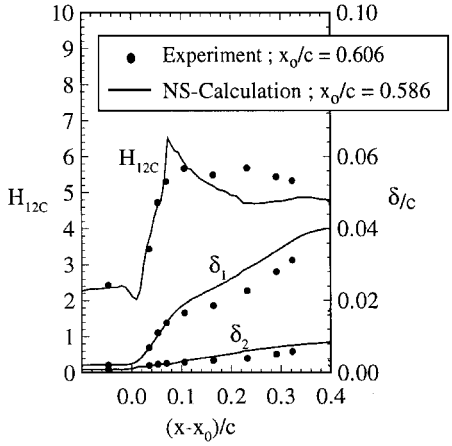

Fig. 3 Compressible boundary-layer data on suction surface at $M_1 = 1.5$.

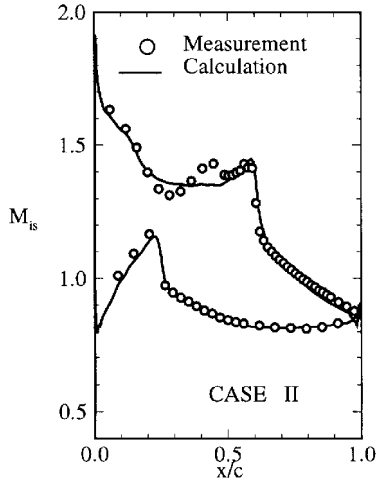

Fig. 4 Isentropic profile Mach number distribution at $M_1 = 1.43$ and $p_2/p_1 = 2.15$.

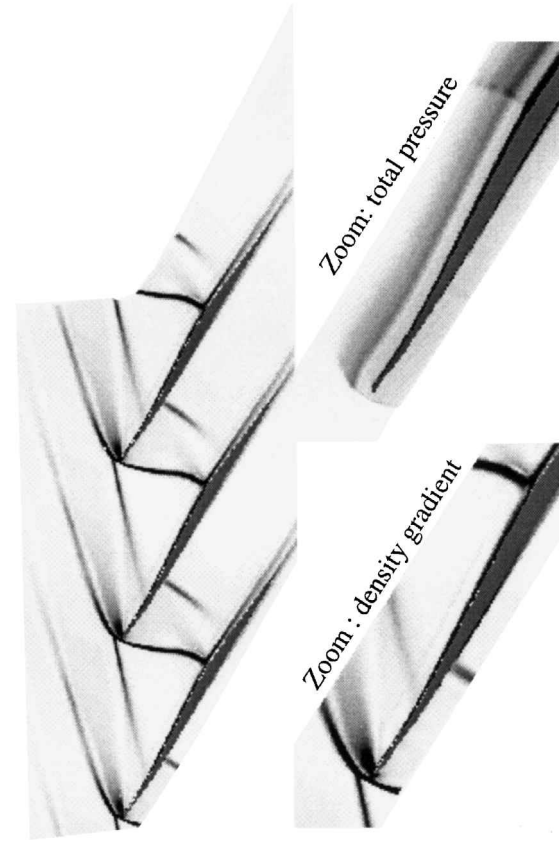

Fig. 5 Density gradient contours at $M_1 = 1.43$ and $p_2/p_1 = 2.15$.

resultant AVDR for the calculation was 0.94, giving a slightly divergent stream tube. In this numerical simulation, the shock-induced boundary-layer separation is well predicted, and the calculated flowfield shows the same shock configuration as observed in the schlieren photograph of the experiment (Fig. 2). Discrepancies in the measured and calculated suction surface Mach number distributions between 25 and 50% of chord are caused by some three-dimensional disturbances in the experiment, emanating from the leading-edge side wall corner region. It seems that their impact on the strong interaction mechanism, which happens farther downstream, is weak and can be ignored. Typical for the precompression design are the compression waves above the concave suction side, which converge in front of the leading-edge bow shock of the neighboring blade. This reduces the Mach number immediately in front of the detached bow shock (the center panel of Fig. 2). Furthermore the classical lambda shock above the separated boundary layer and the Mach reflection with its shock bifurcation points is excellently simulated. Even the so-called kink pressure rise,[2] which is observed between the minimum pressure immediately ahead of the interaction and a kink in the pressure distribution near the separation point at $x/c \approx 0.63$ (right-hand panel of Fig. 2), is predicted correctly. This is because the separation point and the displacement effect of the viscous ramp underneath the lambda shock are accurately simulated.

Corresponding integral suction surface boundary-layer data derived from a pitot survey and the numerical simulation are shown in Fig. 3. The compressible form factor H_{12c} and the displacement thickness δ_1 and momentum thickness δ_2 are plotted from the start of the shock interaction to the trailing edge. The rapid growth of the boundary-layer thickness and form factor underneath the shock is predicted very well and shows only small differences farther downstream in the separated region. No reattachment was observed either in the experiment or in the calculation. In spite of this complete separation, the numerical calculations achieved a converged solution.

Inlet Mach Number $M_1 = 1.43$

Another detailed comparison with experiments was performed at an inlet Mach number of 1.43 with lower boundary-layer loading. Figure 4 shows the profile isentropic Mach number distribution, and Fig. 5 shows the corresponding simulated distribution of density gradients within the flowfield (numerical schlieren picture).

Schlieren observation is a well-established experimental method to analyze and to interpret shock structures and boundary layers in transonic flows. A corresponding numerical method can easily be obtained from the numerical results by defining a density gradient like $|\partial\rho/\partial x| + |\partial\rho/\partial y|$. This not only enables a qualitative comparison of experimental and numerical results over the entire flowfield but also gives a deeper insight into many flow details than the Mach number contour plots shown so far. In comparison with the flow discussed earlier, with an inlet Mach number of 1.5 and a complete suction surface separation from the shock to the trailing edge, here only a local separation with reattachment is observed. The developed lambda shock is much smaller, which means the shock bifurcation point is closer to the surface. Overall data obtained from the measurements agree very well with the calculation results (case 2, Table 1). This was also achieved at a lower inlet Mach number of 1.37 (case 3, Table 1). A special adjustment of the AVDR value was not necessary to match the experimental shock positions for either case 2 or case 3.

Wake traverse data corresponding to the flow condition at $M_1 = 1.43$ are shown in Fig. 6. The total pressure loss distributions agree fairly well. Not only the viscous losses, originating from the boundary layer, but also the shock losses outside of the wake are well predicted. The local loss maximum at the side of the wake at $\eta/t = 0.2$, also predicted by Kunz and Lakshminarayana,[6] has one origin far upstream near the leading edge, where the oblique precompression shock intersects the detached bow shock. About 3% of chord away from the suction surface the bow shock, losses are higher than those close to the surface (Fig. 5). Furthermore, the shock losses of the lambda shock close to the edge of the boundary layer are lower than those farther away.

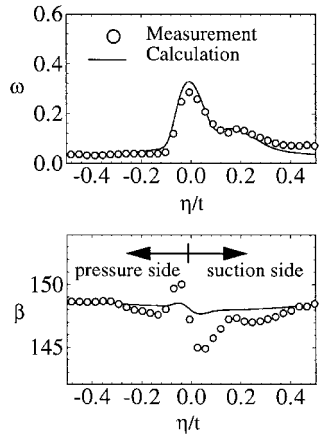

Fig. 6 Total pressure loss coefficient and flow angle distribution at 28% axial chord behind exit plane at $M_1 = 1.43$.

Unlike the total pressure loss, the calculated flow angle distribution across the wake does not match the measurements. With other Navier–Stokes solvers and different cascades, we also observed that the flow angle variation across the wake is decaying too fast in the streamwise direction. Even on finer meshes the results are not improving. It seems that there still is an error in simulating the flow entrainment and mixing process. It is hypothesized that these differences may occur due to ignoring unsteady effects, which are always present in the wake mixing region. Nevertheless the mean values are calculated correctly, as can be seen in Table 1.

Figure 7 shows a comparison of measured and calculated suction surface boundary-layer profiles, one from ahead of and three from behind the shock impingement point. Both measured and calculated Mach number profiles have been determined using the local total pressure and a constant static pressure from the wall. Ahead of the shock a typical turbulent profile with a form factor H_{12C} of 2.3 developed at $x/c = 0.55$. Agreement between simulation and experiment is good, and even behind the shock the shape of the boundary-layer profiles are fairly well predicted. Only the shear layer downstream of the lambda shock bifurcation point, which is clearly visible in the experiment, is slightly smeared out by the simulation, and the calculated point of reattachment seems to be earlier than in the experiment.

Discontinuities Across Passage Shock Wave

Boundary-layer development is only one aspect of the shock-wave/boundary-layer interaction mechanism. It is obvious that a boundary-layer simulation will not be accurate if the quality and accuracy of the outer inviscid flowfield calculation do not correspond to the accuracy of the turbulence model used.[14]

For this reason, the shock structure and the calculated distributions of Mach number and flow angle across the first passage shock

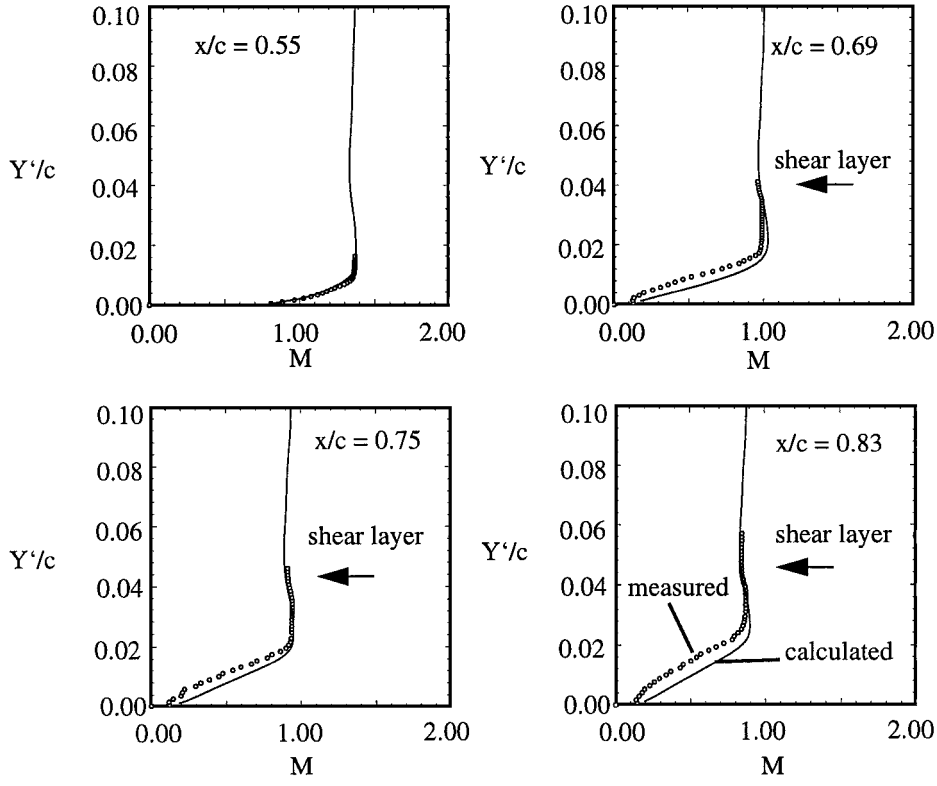

Fig. 7 Suction surface boundary-layer profiles at $M_1 = 1.43$ and shock position $x_s/c \approx 0.63$.

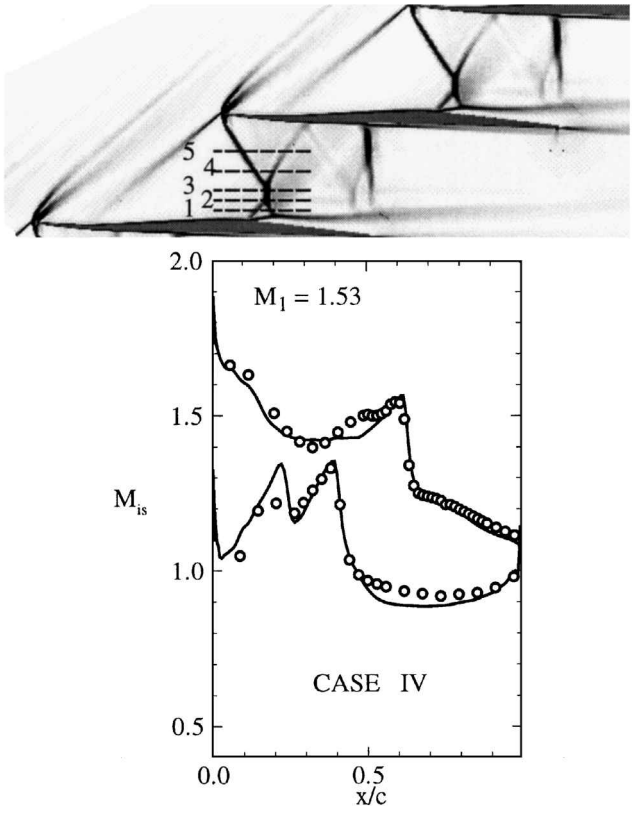

Fig. 8 Calculated density gradients and profile Mach number distribution at $M_1 = 1.53$ and $p_2/p_1 = 2.3$.

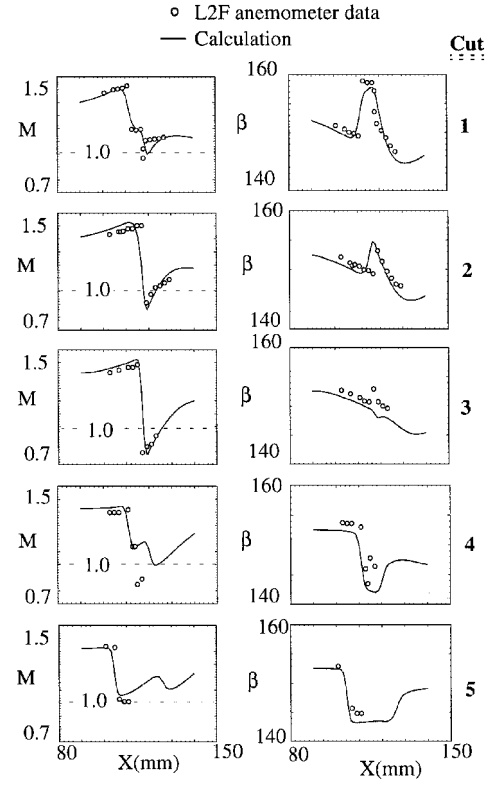

Fig. 9 Mach number and flow angle distribution across lambda and oblique passage shock at $M_1 = 1.53$.

are compared with corresponding detailed laser-2-focus anemometer data from an experiment.[5,15] In Fig. 8 the corresponding profile isentropic Mach number and density gradient distributions are provided. Inlet and outlet data are listed in Table 1 (case 4). Again, the AVDR value had to be adjusted to achieve identical shock wave positions.

As can be seen in Fig. 8, there is a strong SWBLI with a separation reaching from the interaction region to the trailing edge. Locations of the cuts through the shocks have been marked by dashed lines in the flowfield in Fig. 8 and correspond to the following heights: cut 1, $y = 5$ mm; cut 2, $y = 10$ mm; cut 3, $y = 15$ mm; cut 4, $y = 25$ mm; and cut 5, $y = 35$ mm, where $y = 0$ mm is the suction surface point at $x_{LE} = 100$ mm. Cuts 1–3 intersect the lambda shock, and cuts 4 and 5 intersect the oblique passage shock. Mach number and flow direction distributions along the cuts are shown in Fig. 9. Measured discontinuities of both Mach number and flow angle are very sharp and reproduce the shock within 1–2 mm. The flow solver with its TVD scheme captures the discontinuities of the lambda shock within about three to four grid lines, which corresponds to about 3–4 mm.

Preshock and postshock levels are accurately simulated, and even the postshock expansion around $M = 1.0$, which is typical for the SWBLI process, is well predicted. Only the lambda shock discontinuities (cut 1) are smeared out a little.

Finally, however, this excellent agreement for the shock discontinuities could be achieved only because for this specific case the boundary conditions (especially AVDR and back pressure) have been adjusted to obtain the same shock position. Deviations in the measured and calculated exit flow angles and pressure increase especially for $M_1 = 1.5$ and 1.53 (see Table 1) indicate the discrepancies due to the different AVDR values. The applied AVDR manipulations in these two cases may have been necessary to compensate for some underprediction of the boundary-layer separation and blockage effects, which occur particularly at the higher preshock Mach numbers.

Influence of Axial Stream Tube Convergence

The AVDR, which indicates the axial stream tube convergence, has a great influence on the flow behavior, especially on flow turning,

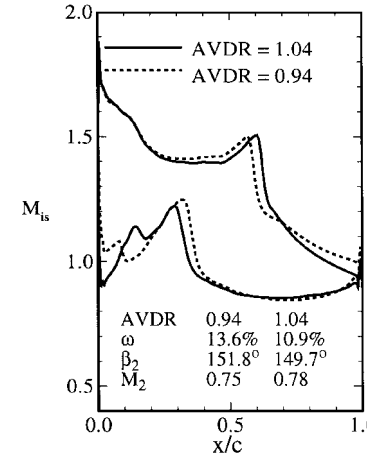

Fig. 10 Influence of AVDR on isentropic profile Mach number distribution and cascade performance at $M_1 \approx 1.5$ and $p_2/p_1 \approx 2.27$.

pressure ratio, and not least the shock-wave/boundary-layer interaction mechanism. In previous experiments it has been observed that shock wave position, shock strength, and the loss mechanism vary considerably with AVDR, although blade loading with the static pressure rise was kept constant. The present Navier–Stokes calculations confirm the observed flow behavior. Furthermore, they help to clarify the fluid mechanic mechanism that designers should keep in mind when they intend to improve transonic fan performance.

In Fig. 10 the profile isentropic Mach number distribution of two calculations with different AVDRs is shown. All other boundary conditions, i.e., exit pressure, were held constant. The calculation with AVDR $= 0.94$ shows a strong SWBLI with a lambda shock and a significant separation. Increasing the AVDR to 1.04 leads to a slight upstream movement of the second passage shock on the pressure side and thereby a reduction of the preshock Mach number. Also, the Mach number ahead of the bow shock and the oblique passage shock, visible in the suction surface Mach number distribution of Fig. 10 between 20 and 58% of chord, is slightly reduced. Unlike the second passage shock, which moves upstream to lower preshock Mach numbers, the oblique shock extends farther downstream (see the upper passage on the left of Fig. 11). Because

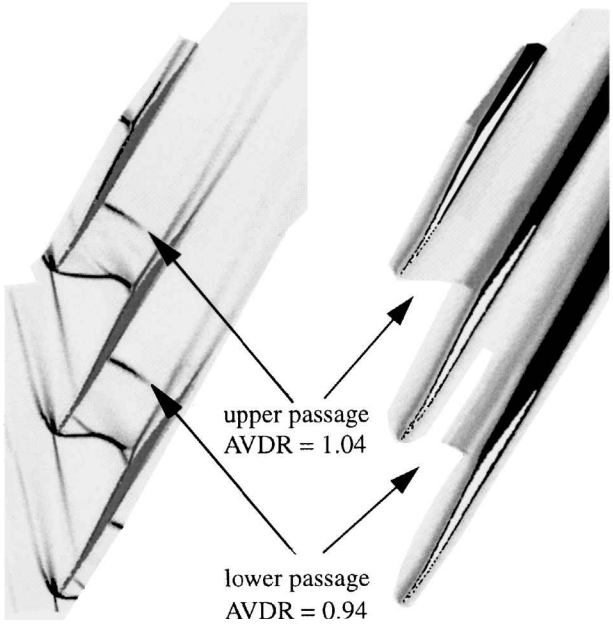

Fig. 11 Influence of AVDR, calculated density gradients (left) and total pressure contours (right), at $M_1 \approx 1.5$ and $p_2/p_1 \approx 2.27$.

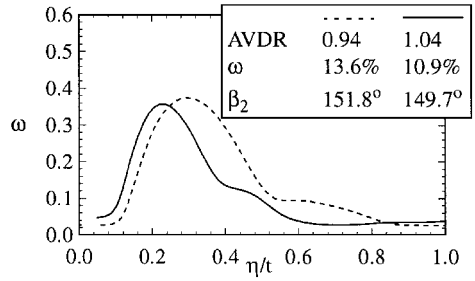

Fig. 12 Loss coefficient distribution across the wake for different AVDR ($M_1 \approx 1.5, p_2/p_1 \approx 2.27$, and $\xi/c_{ax} = 1.44$).

of a weaker shock, the boundary-layer interaction and the shock-induced separation are less strong, and the lambda shock, which forms near the blade surface, is much smaller.

Overall, increasing AVDR reduces shock losses and the viscous losses resulting from SWBLI on the blade pressure side and particularly on the suction side. Calculated total pressure contours, provided in Fig. 11 (on the right), clearly show the variation in wake width and the different total pressure loss mechanisms behind the lambda shock when AVDR is changed. Wake width and shock losses outside of the wake are considerably reduced when AVDR is increased (Fig. 12), resulting in a reduction of overall losses from 13.6 to 10.9% and a simultaneous variation of the exit flow angle β_2 corresponding to an increase in flow turning of about 2 deg.

Influence of Inlet Mach Number

This section shows a numerical study of the inlet Mach number influence on the cascade flow field, overall performance data like inlet and exit flow angle, static pressure rise, and loss coefficient. Typical for such rotor blade elements is that they usually operate at an inlet flow angle that corresponds to a flow condition with maximum mass flow. For supersonic inflow, maximum mass flow is given either if the cascade chokes due to throat area blockage or at higher inlet Mach numbers when the supersonic flow into the cascade blade passage is started and the so-called unique incidence condition is established. To achieve these conditions, the back pressure is set to a relatively low value, and this has been kept constant for all of the calculations at different inlet Mach numbers ($p_2/p_{t1} = 0.64$). Figure 13 shows the calculated cascade flowfield for inlet Mach numbers of 1.28, 1.37, 1.43, and 1.49, which correspond to conditions near 85, 90, 95, and 100% of compressor speed. At $M_1 = 1.28$ the cascade operates with unstarted choked flow, resulting in a relatively high

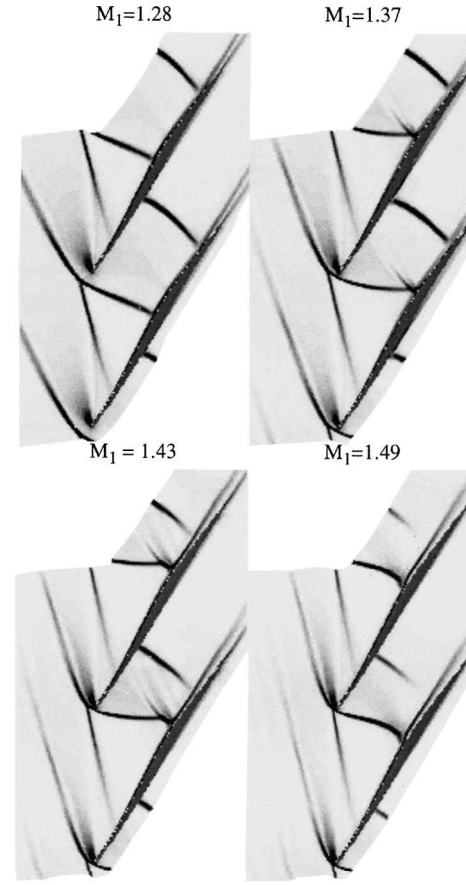

Fig. 13 Calculated density gradients for different inlet Mach numbers at constant back pressure $p_2/p_{t1} = 0.64$ and constant AVDR = 1.02.

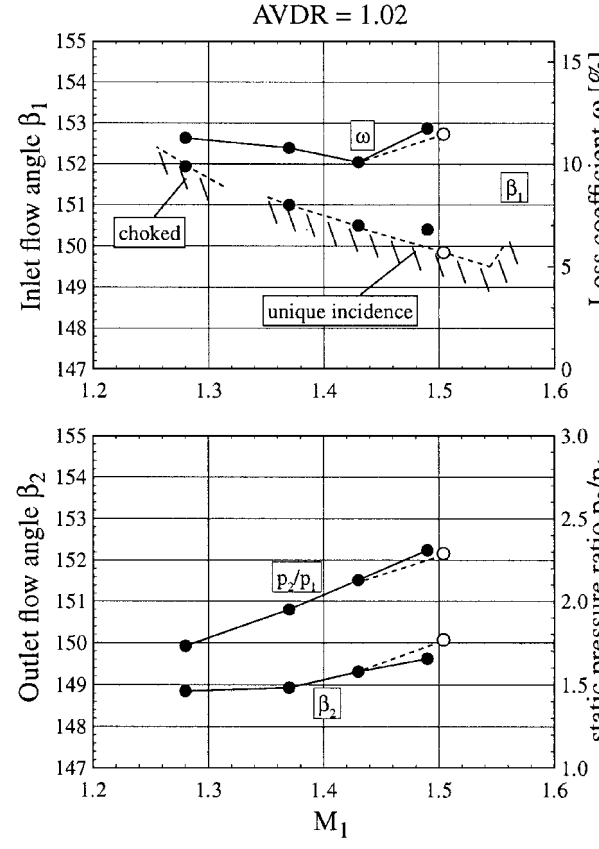

Fig. 14 Inlet/outlet flow angle, loss coefficient, and static pressure ratio for different inlet Mach numbers.

incidence, whereby the bow shock detaches from the blade leading edge. At $M_1 = 1.37$ and 1.43 the supersonic flow is started into the blade passage, forming an oblique shock at the entrance.

For $M_1 = 1.49$ (bottom right of Fig. 13) the prescribed back pressure is slightly too high for maximum mass flow or minimum flow angle and pushes the passage shock farther upstream to form a nearly normal shock at passage entrance. A minimum flow angle again could be achieved by reducing the back pressure to $p_2/p_{t1} = 0.62$ (open symbol in Fig. 14).

Calculated cascade flow angles β_1 and β_2, as well as performance data including the loss coefficient and static pressure ratio of the flow cases discussed earlier, are plotted in Fig. 14 against the inlet Mach number. An interesting feature of the precompression blade is that the minimum inlet flow angle (unique incidence, at the top of Fig. 14) decreases continuously when the inlet Mach number is increased. This unique incidence behavior is typical for a blade with concave suction surface curvature along its front portion.[4]

Conclusions

A two-dimensional Navier–Stokes solver has been applied to the supersonic/transonic flow past a low turning compressor cascade and validated against experimental data obtained in a supersonic cascade facility.

Investigations have shown that the numerical solver provides an accurate resolution of the supersonic flowfield and an excellent reproduction of the complex shock wave pattern in front of and within the blade passage. The region of strong shock-wave/boundary-layer interaction is adequately simulated by a one-equation turbulence model for shock-induced boundary-layer separation both with and without reattachment. Also, the overall cascade performance data such as shock losses and viscous losses are well predicted. Only a small deficit exists in simulating the wake mixing process, where the code underpredicts the flow entrainment process and thus the local flow angle variation across the wake. For very highly loaded flows with severe shock-induced separations, however, a satisfactory agreement between experiment and numerical simulation could be obtained only when the back pressure and especially the simulated axial stream tube thickness variation was adjusted in such a way that the strong pressure rise underneath the passage shocks fits the experiments. This seemed to be necessary to force the boundary-layer separation to be strong enough to give the right blockage effect.

Generally, the code is an excellent tool to support the experimental investigations and analysis of complex transonic flow phenomena and to perform design and parameter studies. For example, it has been shown clearly that an increase in axial stream tube convergence provides a relief of the SWBLI region and a clear reduction of both shock and viscous losses.

References

[1] Kooi, J. W., "Influence of the Free-Stream Mach Number on Transonic Shock-Wave/Boundary Layer Interaction," National Aerospace Lab. NLR, MP-78013 U, Amsterdam, May 1978.

[2] Atkin, C. J., and Squire, L. C., "A Study of the Interaction of a Normal Shock Wave with a Turbulent Boundary Layer at Mach Numbers Between 1.3 and 1.55," *European Journal of Mechanics, B/Fluids*, Vol. 11, No. 1, 1992, pp. 93–118.

[3] Bell, R. M., and Fottner, L., "Investigations of Shock/Boundary-Layer Interaction in a Highly Loaded Compressor Cascade," American Society of Mechanical Engineers, ASME Paper 95-GT-84, 1995.

[4] Schreiber, H. A., "Shock-Wave Turbulent Boundary Layer Interaction in a Highly Loaded Transonic Fan Blade Cascade," *Loss Mechanisms and Unsteady Flows in Turbomachines*, CP-571, AGARD, Jan. 1996 (Paper 17).

[5] Schreiber, H. A., and Starken, H., "An Investigation of a Strong Shock-Wave Turbulent Boundary Layer Interaction in a Supersonic Compressor Cascade," *Journal of Turbomachinery*, Vol. 114, July 1992, pp. 494–503.

[6] Kunz, R. F., and Lakshminarayana, B., "Explicit Navier–Stokes Computation of Cascade Flows Using the $k-e$ Turbulence Model," *AIAA Journal*, Vol. 30, No. 1, 1992, pp. 13–22.

[7] Eulitz, F., Engel, K., and Pokorny, S., "Numerical Investigation of Inviscid and Viscous Interaction in a Transonic Compressor," *Loss Mechanisms and Unsteady Flows in Turbomachines*, CP-571, AGARD, Jan. 1996 (Paper 38).

[8] Eulitz, F., Engel, K., and Gebing, H., "Application of a One-Equation Eddy-Viscosity Model to Unsteady Turbomachinery Flow," *Engineering Turbulence Modelling and Experiments 3*, edited by W. Rodi and G. Bergeles, Elsevier Science, Amsterdam, 1996, pp. 741–751.

[9] Roe, P. L., "Approximative Riemann Solvers, Parameter Solvers and Difference Schemes," *Journal of Computational Physics*, Vol. 43, 1981, pp. 357–372.

[10] van Leer, B., "Towards the Ultimate Conservation Difference Scheme V, A Second-Order Sequel to Godunov's Method," *Journal of Computational Physics*, Vol. 32, 1979, p. 101.

[11] Spalart, P. R., and Allmaras, S. R., "A One-Equation Turbulence Model for Aerodynamic Flows," AIAA Paper 92-0439, 1992.

[12] Giles, M. B., "UNSFLO: A Numerical Method for the Calculation of the Unsteady Flow in Turbomachinery," Gas Turbine Lab., GTL Rept. 205, Massachusetts Inst. of Technology, Cambridge, MA, 1990.

[13] Engel, K., Eulitz, F., Faden, M., and Pokorny, S., "Validation of Different TVD Schemes for the Calculation of the Unsteady Turbomachinery Flow," *Proceedings of the International Conference on Numerical Methods in Fluid Dynamics ICNMFD 94*, Bangalore, India, July 1994.

[14] Drikakis, D., and Durst, F., "Investigation of Flux Formulae in Transonic Shock Wave/Turbulent Boundary Layer Interaction," *International Journal for Numerical Methods in Fluids*, Vol. 18, 1994, pp. 385–413.

[15] Schreiber, H. A., "Experimental Investigation on Shock Losses of Transonic and Supersonic Compressor Cascades," *Transonic and Supersonic Phenomena in Turbomachines*, CP-401, AGARD, March 1987 (Paper 11).

K. Kailasanath
Associate Editor